ADVANCED ENERGY MATERIALS
www.advenergymat.de

Bipolar Membranes With Controlled, Microscale 3D Junctions Enhance the Rates of Water Dissociation and Formation

*Tianyue Gao, Leanna Schulte, Langqiu Xiao, Eisuke Yamamoto, Amy S. Metlay, Colton J. Sheehan, Sariah Marth, Heemin Park, Sayantan Sasmal, Francisco J. Galang, Chulsung Bae, Adam Z. Weber, Shannon W. Boettcher, and Thomas E. Mallouk**

A soft lithographic method is developed for making bipolar membranes (BPMs) with catalytic junctions formed from arrays of vertically oriented microscale cylinders. The membranes are cast from reusable polydimethylsiloxane (PDMS) molds made from silicon masters, which are fabricated on 2″ to 4″ wafer scales by nanosphere lithography. High-aspect-ratio junctions are made on a length scale similar to the thickness of optimized catalyst layers for water dissociation, creating a platform for probing the dual effects of catalysis and local electric field at the microscale BPM junction. Optimized polymer materials and nanoscale metal oxide catalysts are used in this study. 3D BPMs are tested under reverse and forward bias conditions, exhibiting superior performance relative to their 2D counterparts. Under forward bias in H_2-O_2 fuel cells, 3D BPMs achieve a current density of 1500 mA cm^{-2}, ≈7 times higher than 2D membranes made from the same materials.

1. Introduction

Over the past few decades, ion-exchange membranes have become increasingly important for practical applications in electrochemical separations and energy conversion.[1,2] At the heart of these systems are anion exchange layers (AELs) or cation exchange layers (CELs), in which the ionic groups immobilized in the membrane are positively or negatively charged, respectively.[3,4] When an AEL and a CEL are laminated together, a bipolar membrane (BPM) is formed, and, in the absence of a supporting electrolyte, an internal electric field forms across the interfacial junction.[5] Using a BPM as a separator in an electrochemical cell offers advantages over a single monopolar AEL or CEL electrolyte because the BPM enables the device to operate with each electrode in a different pH environment.[6,7] Consequently, BPMs hold potential for a variety of applications in energy conversion, storage, and environmental separations.[8,9] The integration of BPMs into devices has become a crucial component in various processes,[10] including electrodialysis for the production of inorganic acids and bases,[11] redox-flow batteries,[8] wastewater decalcification,[12] flue gas desulfurization,[13]

T. Gao, L. Schulte, L. Xiao, A. S. Metlay, C. J. Sheehan, T. E. Mallouk
University of Pennsylvania
Department of Chemistry
231 S 34th St, Philadelphia, PA 19104, USA
E-mail: mallouk@sas.upenn.edu

E. Yamamoto
Department of Materials Chemistry & Institute of Materials and Systems for Sustainability (IMaSS)
Nagoya University
Nagoya 464-8601, Japan

S. Marth, H. Park, C. Bae
Department of Chemistry and Chemical Biology
Rensselaer Polytechnic Institute
Troy, NY 12180, USA

S. Sasmal, S. W. Boettcher
Department of Chemistry and Biochemistry and the Oregon Center for Electrochemistry
University of Oregon
Eugene, OR 97403, USA

F. J. Galang, A. Z. Weber
Energy Storage and Distributed Resources Division
Lawrence Berkeley National Laboratory
Berkeley, CA 94720, USA

S. W. Boettcher
Department of Chemical & Biomolecular Engineering and Department of Chemistry
University of California
Berkeley
Energy Storage and Distributed Resources Division
Lawrence Berkeley National Laboratory
Berkeley, CA 94720, USA

The ORCID identification number(s) for the author(s) of this article can be found under https://doi.org/10.1002/aenm.202404285

DOI: 10.1002/aenm.202404285

artificial photosynthesis,[14] CO_2 and bicarbonate reduction,[15,16] CO_2 capture,[17] water electrolysis,[18] and fuel cell applications.[19]

BPM performance is often constrained by the rate of the water-based reaction occurring at the AEL|CEL junction. For instance, under reverse bias, ions are dialyzed from the junction, and water dissociation ($H_2O \rightarrow H^+ + OH^-$) begins to occur, requiring an applied potential.[20] Water dissociation is essential for BPMs because it produces H^+/OH^- ions that carry the ionic current flow through the system and replenish ions consumed at the cathode and anode to enable continuous operation at differential pH conditions.[21] Undesired overpotentials are also observed in existing forward-biased BPM operations in which water formation occurs at the junction ($H^+ + OH^- \rightarrow H_2O$). Thus, electrochemical performance strongly depends on the choice of catalyst in the BPM junction.[22] To enhance the performance of BPMs and achieve more efficient devices like water electrolyzers and fuel cells, further research is needed to understand design principles in the BPM junction. Previous research has primarily concentrated on optimizing catalyst designs to achieve the highest current densities with the lowest overpotential for water dissociation/formation.[22,23] However, the effects of the membrane-catalyst interface are still being explored, particularly regarding the roles of catalytic and electric field effects at the junction. We believe it is critical to design a system to understand these interfacial effects, which is why we are focusing on 3D BPMs, distinguishing them from traditional 2D BPMs.

2D planar BPMs are often prone to issues like delamination, dehydration, or flooding at the junction, limiting their efficiency.[24] Recently, researchers have reported methods to improve junction lamination[25] and increase the contact area between AEL and CEL materials.[24,26–30] In 2017, Pintauro and coworkers reported a radically new method for improving junction design, using a dual nanofiber electrospinning technique to interpenetrate AEL and CEL polymer fibers.[24] The resulting BPMs demonstrated improved adhesion between the two polymer layers and effectively minimized the issues of water depletion and flooding at the junction under reverse and forward bias conditions, respectively. Although electrospinning significantly increases the interfacial area, it results in a random distribution of AEL/CEL fibers in the junction region making it difficult to quantify the contacting area. This random orientation also makes it challenging to quantitatively correlate electrochemical performance with the junction area and to study the electric field effects at the interface.

In addition, research has been conducted on controlled micropatterning of the surface of monopolar membranes,[31–34] as well as BPMs. For example, Arges and co-workers used photolithography to create master templates for patterning 3D BPMs with well-ordered arrays of cylindrical junctions.[7] Their experiments showed that increasing the junction surface area increased the apparent rate constant for water dissociation in reverse bias, resulting in a lower onset overpotential. While their methods created BPMs with quantifiable junction areas, the lithographic features ranged from tens to hundreds of micrometers. This is significantly larger than the optimized thickness of the water dissociation catalyst layer, which recent literature reports to be around hundreds of nanometers to ≈1 micron depending on the component of the catalysts.[23]

We report here a nano-/microsphere lithographic method for fabricating 3D BPMs, creating high-aspect-ratio vertical features at the BPM interface. These features are dimensionally close to the thickness of the catalyst layer, which is ≈1 µm, creating a well-defined structure for studying the dual effects of catalysis and interfacial electric field. The catalyst coverage was independently controlled, and the junction features remained intact after the tests. Our findings identify trends between BPM surface area and the performance of the water dissociation and formation in these high-surface-area systems. These trends can be compared with 2D finite-element modeling of the structured BPM interface using the Poisson-Nernst-Planck formalism detailed in the Supplementary Information sections.

2. Results and Discussion

To study the relationship between BPM interfacial area and their electrochemical characteristics, we developed a nano-/microsphere lithographic method for fabricating geometrically well-defined 3D BPMs over the length scale of interest. In the 3D BPMs, the AEL is patterned into an array of vertically oriented cylinders. The catalyst and CEL are then deposited onto the AEL to create an interdigitated structure (**Figure 1**). Experimental details can be found in the Methods section. Briefly, we started the fabrication process by assembling a monolayer of uniform polystyrene spheres on the surface of a silicon wafer. These particles, which formed a close-packed monolayer, were then reduced in size by plasma etching. The exposed silicon surface between the then-separated particles was vertically etched, creating a uniform pattern of cylindrical pillars. This process converted the silicon wafer into a master for subsequent fabrication of the 3D BPMs (Figure S1, Supporting Information). The height of the cylindrical structures, which directly influence the interfacial area of the resulting BPM, could be adjusted by varying the number of plasma etching cycles. A fresh mixture of silicon elastomer base and the curing agent was cast onto the silicon template. Once cured, it served as a reusable and organic solvent-tolerant polydimethylsiloxane (PDMS) template that could be used repeatedly to prepare patterned AELs (Figures S1 and S2, Supporting Information).

To create the patterned AELs, an AEL-DMSO solution was cast atop the PDMS mold, and the solvent was evaporated thoroughly at 70 °C. For control studies without interfacial patterning, the AEL was cast on a flat 2D PDMS template. After the AEL was peeled away from the mold, TiO_2 or SnO_2 catalyst nanoparticles, mixed with an equal weight of acetylene carbon black (ACB) and dispersed in isopropanol, were sprayed onto the AEL.[23] Finally, a commercial Nafion film, serving as the CEL, was pressed onto the catalyst layer to complete BPM. A more detailed description of the fabrication steps is given in the Materials and Methods section.

To cast the AEL from the solution phase, it was imperative that the polymer was soluble in a polar organic solvent, such as DMF, ethanol, or DMSO. This 3D BPM method offers flexibility, enabling high aspect-ratio membranes to be cast from a variety of different materials. Several AEL materials were tested, including mTPN1,[35,36] AP3, PiperION, and QAPPT[37] (**Figure 2**; Figure S3, Supporting Information). These survey experiments indicated that the mTPN1 polymer was particularly

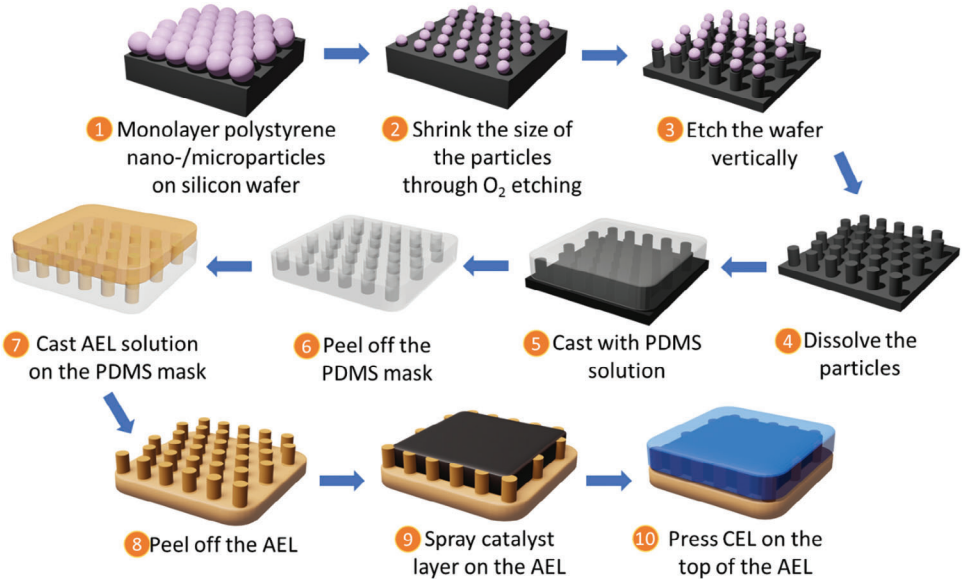

Figure 1. Process flow for fabricating geometrically controlled 3D BPMs over the length scales of interest.

well-behaved, demonstrating both excellent mechanical integrity of the 3D pattern and high ionic conductivity in electrochemical testing.[35,36]

Figure 2 shows SEM images of mTPN1 AELs with different cylinder heights, along with a plane-view image of the membrane surface to illustrate the pattern's uniformity. In general, these images validate the success and reliability of the method in producing 3D AELs with systematically defined micropatterns, which was a critical step in obtaining geometrically well-defined BPM interfacial junctions. To calculate the interfacial surface areas of the series of BPMs, we used the pitch of the array, which is defined by the original 3 μm diameter of the polystyrene particles, and the sidewall area of the cylinders, as described in Equation S1 (Supporting Information). To clarify terminology used in later sections, we employ the symbol "×" to indicate how many times larger the 3D BPM surface area was compared to a planar BPM. For example, for a 3D AEL with 2 μm high cylinders, the surface area of the resulting BPM junction was approximately double that of a 1 × 1 cm^2 planar BPM (a 2D BPM is denoted as 1.0×), and therefore, we denote this BPM as "2.0×." Systematically tuning the height of the pattern via the number of etching cycles of the silicon wafer enabled control over the surface area ratio. While maintaining the diameter of the cylindrical structure at ≈1.2 μm for all 3D BPMs in this study, the surface area of the interfacial junction increased proportionally with the height of the 3D structures. Here, we fabricated and characterized structures with heights of 0.9, 2.0, and 4.1 μm which we refer to as 1.4×, 2.0×, and 3.0× BPMs based on their surface area relative to a 2D (1.0×) BPM.

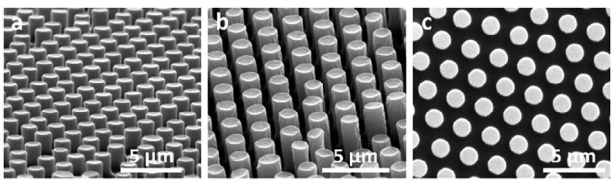

Figure 2. Scanning electron micrographs (SEM) of the 3D mTPN1 AELs: a,b) Cross-section images of the AEL with different cylinder heights: (a) 2.0 μm, and (b) 4.1 μm. c) The top-down image of the sample is shown in (a).

A critical feature of high-performing BPMs is a controlled coating of water dissociation/formation catalyst at the AEL|CEL junction. In fabricating 3D BPMs, it was nontrivial to ensure a uniform catalyst coating atop the highly corrugated interfacial junction. Initial attempts involved attaching graphene oxide (GO) flakes, known for their excellent water dissociation activity,[27,38] on the AEL surface. However, these flakes typically have lateral dimensions of micrometers and did not efficiently cover the surface of the patterned AEL layer. An alternative approach was to utilize metal-oxide nanoparticles as catalysts by spraying a mixture of the metal oxide, e.g. TiO_2 or SnO_2,[6] as nanoparticles suspended in isopropanol and ionomer onto the AEL surface. However, these attempts revealed that micrograms of metal oxide particles per cm^2 were insufficient to uniformly cover the entire surface structure, as depicted in Figure S4 (Supporting Information). Increasing the mass loading of TiO_2 was considered; however, as shown by Chen et al.,[23] an excessively thick layer of metal oxide particles, specifically in the wells of our 3D structure, would result in high resistance and hinder water dissociation performance.

In light of these challenges, we mixed commercial anatase TiO_2 or SnO_2 nanoparticles made by low-temperature hydrolysis of $SnCl_4$,[39] with an equal weight of acetylene carbon black (ACB), dispersed in isopropanol. ACB, being electronically conductive, augmented the catalyst layer's volume without significantly increasing resistance.[23] **Figure 3** shows a cross-sectional image of the AEL after the catalyst was sprayed on top. A well-dispersed mixture of metal oxide and ACB effectively filled the gaps between the cylinders and formed a uniform layer. A more detailed description of the spraying process is provided in the Experimental Section.

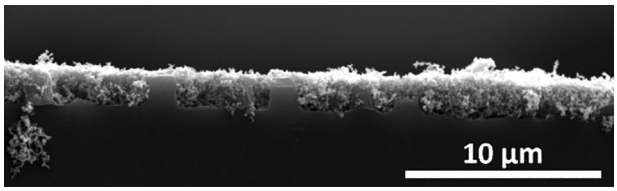

Figure 3. SEM of the 3D AELs after ACB/TiO_2 was sprayed onto the 3D structured surface.

The AEL with catalyst was soaked in 1 M KOH at 70 °C overnight for ion exchange before placing a Nafion film over the catalyst layer. The entire assembly was then hot-pressed to ensure a robust interfacial connection between the AEL and CEL in the junction region. Cross-sectional SEM confirmed that BPMs with and without catalyst layers maintained their interfacial structures after hot pressing and electrochemical testing (**Figure 4**; Figure S5, Supporting Information). In general, the homemade mTPN1 AEL had a thickness of 42 ± 3 µm, with a catalyst layer just covering all the patterned microstructures. The commercial Nafion 212 layer was 50 µm thick, resulting in a BPM with a total thickness of less than 100 µm. These BPMs could be easily handled before and after tests, in both wet and dry states, without delamination or cracking.

2.1. Electrochemical Characterization

We utilized an H-pump cell to gain a fundamental understanding of the water dissociation and formation reactions at the BPMs junction.[40] This membrane-electrode assembly (MEA) system includes BPMs, Pt black ionomer-coated carbon paper as gas diffusion layer (GDL), Teflon gaskets, flow fields, etc. as illustrated in **Figure 5**a. The cell fixture was connected to a fuel-cell-test station with forming gas (5% H_2 in N_2) supplying to both the cathode and anode at 60 °C and a flow rate of 0.5 L min^{-1}. The presence of H_2 enabled the system to transduce electrical current at the electrodes into the ionic current, which either produced H^+ at the CEL under forward bias or consumed OH^- and produced water at the AEL under reverse bias (Figure 5b).[41] Here, we define the forward bias condition as one in which positively and negatively charged ions flow into the junction. In reverse bias, water dissociation occurs in the junction, and positively and negatively charged ions flow into the CEL and AEL, respectively. H-pump cell systems minimize the influence of electrode reactions on BPM performance, as they primarily involve hydrogen oxidization and reduction with platinum, which exhibit very low overpotentials. In addition, this testing format allowed us to probe the impedance performance of the BPM using electrochemical methods, without the interference of co-ions that can enter the membrane in an aqueous H-cell that incorporates supporting electrolytes. All forming-gas membrane-polarization experiments were conducted in galvanostatic mode, with a fixed current applied, and the corresponding cell voltage was measured after stabilization.[24]

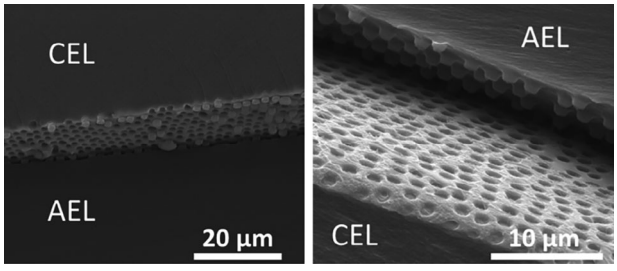

Figure 4. The interfacial surface of a 3D BPM film after intentionally delaminating the AEL and CEL via freeze-drying. The microstructures remained intact even after assembly and electrochemical testing of the BPM. No TiO_2/ACB catalyst was incorporated in the BPM junction in this instance solely to facilitate clear imaging of the membrane structures.

To evaluate the overpotential of the water dissociation and formation reactions, polarization experiments were conducted under both reverse and forward bias conditions with constant applied current densities in the 0–100 mA cm^{-2} range. The resulting current-cell potential (J-E) curves are shown in **Figure 6**. Experimental details can be found in the Supporting Information. The voltage values are IR corrected for series resistances associated with AEL and CEL ion conduction evaluated by EIS, which is detailed in Figure S7 (Supporting Information). Although there are inflection points appearing in the polarization curves, they are likely attributed to changes in mass transfer resistance from GDL. For instance, the EIS of the 1.0× TiO_2/ACB showed two or three distinct semicircles, corresponding to water dissociation/formation resistance, charge transfer, and mass transfer resistance of H_2 and ions at the GDL with the Pt/C catalyst (Figures S8 and S10, Supporting Information). It's important to note that charge and mass transfer resistances are unlikely to significantly impact the polarization curves in the low current density region, as the resistances related to water dissociation are much higher than those associated with mass transfer. Additionally, the cell potential for each sample was higher than the values reported by Chen, et al.,[23] due to the presence of the Nafion ionomer in the catalyst layer (Figure S9, Supporting Information). While the addition of the ionomer slightly increases the impedance of water dissociation and formation reactions, the relative contribution of mass transfer resistance is lowered, as confirmed by EIS (Figure S8b,c Supporting Information), allowing us to clearly observe the differences in water dissociation and water formation impedances from polarization curves. Furthermore, the 3D BPMs demonstrated superior performance compared to their 2D counterparts when ionomers were incorporated into the catalyst layer. This enhancement is likely attributed to the increase in active area in the region adjacent to the AEL. Consequently, the increased surface area of the 3D BPMs contributes to their improved performance compared to 2D BPMs. In the absence of ionomers, however, the polarization curves of 3D and 2D BPMs were comparable, as shown in Figure S9a,b (Supporting Information). This similarity can be explained by considering that, without ionomers, water dissociation occurs catalytically throughout the entire volume of the catalyst rather than being localized to the catalyst/AEM interface. In this context, the longer transport distance associated with the 3D structure may introduce greater resistance from series resistance, as illustrated in Supplementary Figure S9c,d (Supporting Information). Another benefit of incorporating the ionomer in this experimental design is that the electric field is primarily concentrated on the AEL side of the catalyst layer when acidic Nafion is mixed with the catalyst particles, which makes it possible to isolate the effects of the interface

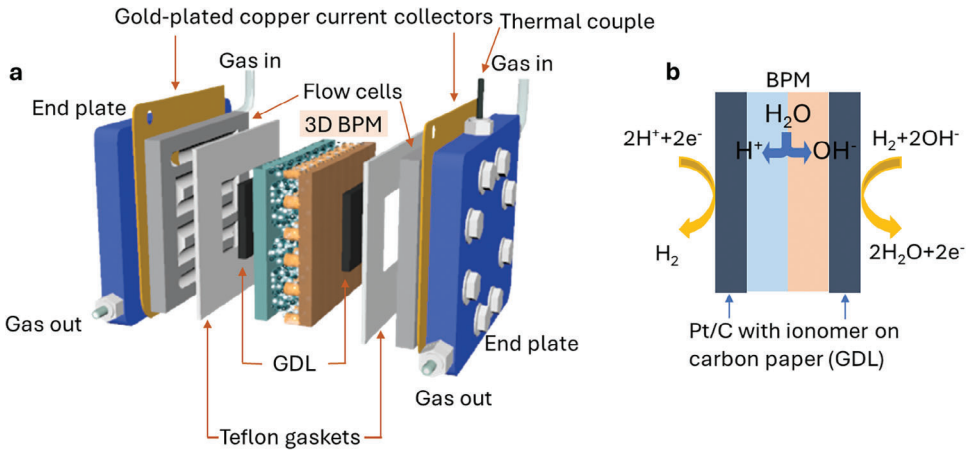

Figure 5. a) Experimental test fixture setup and b) a scheme for the forming gas tests under reverse bias conditions for the water dissociation reaction.

design. Therefore, we are able to qualitatively evaluate the differences in overpotential between samples by comparing the variations in cell voltage at low currents region in these polarization curves. Unless otherwise specified, all metal oxide catalysts were combined with ACB and Nafion ionomer, as described in the Experimental Section.

We then compared the cell voltage of all samples at specific current densities to evaluate the performance of the BPMs. Regardless of the catalyst type, the 3D BPMs with the largest junction area (3.0 × BPMs) exhibited the lowest cell voltages at a given current density within the group. At 60 mA cm^{-2}, the cell voltages required to drive current through the 3.0 × BPMs were ≈50–60% of those needed for the 1.0 × BPMs. These results indicate that introducing a large junction area reduces the overpotential for water dissociation and formation reactions. It appears that the overpotential for water dissociation is lowered due to the increased reaction volume available for water dissociation,[7] particularly along the vertically oriented AEL|catalyst interface (Figure S16, Supporting Information).

We also investigated the effects of introducing a 3D junction on the composition of the catalyst nanoparticles by evaluating the resistances of water dissociation and formation reaction estimated through EIS (Figure S7, Supporting Information). All BPMs containing SnO_2 showed lower resistances than those with TiO_2, indicating that SnO_2 exhibits higher catalytic activity than anatase TiO_2 for both water dissociation and water formation tests. Furthermore, the polarization curves of samples with SiO_2/ACB in the catalyst layer also supported the effects of catalyst compositions (Figure S22, Supporting Information). We also experimentally assessed the performance of a series of 2D and 3D BPMs that did not contain any catalyst, and these exhibited significantly lower current densities compared to those with effective catalysts, e.g. TiO_2 and SnO_2. This highlights that, even with the 3D structuring of the BPM interface, a high-performance water dissociation/formation catalyst is essential for achieving elevated current densities (Figure S22, Supporting Information).

In addition, we compared the resistances measured under 0 and 60 mA DC bias to probe the effects of electric fields (Figure S7Supporting Information). For samples with a low junction area, such as 1.0× and 1.4× samples, the resistance significantly decreased with increased DC bias. In contrast, the resistances of samples with larger junction areas, including 2.0× and 3.0× samples, showed almost no change. These results suggest that electric-field effects are rather weakened when a large junction area is introduced. Given that a large junction area lowers resistances and cell potentials across all catalyst compositions, the

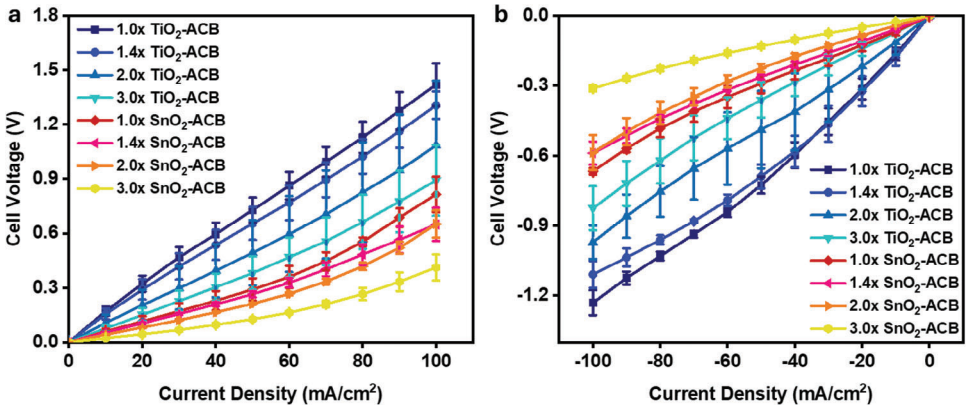

Figure 6. Polarization curves of 2D and 3D BPMs with TiO_2/ACB and SnO_2/ACB catalyst layers in the forming gas test at 60 °C with a flow rate of 0.5 L mi^{-1}n, a) reverse bias, b) forward bias. Error bars correspond to the standard deviation based on a minimum of three trials.

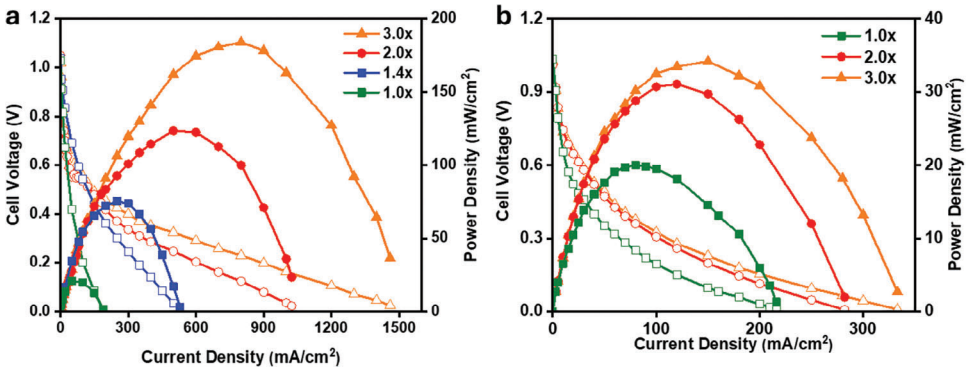

Figure 7. Power-density curves and polarization curves of fuel-cell performance for 2D and 3D BPMs a) with and b) without TiO_2-ACB catalyst layers at the junction. The cell temperature was set at 100 °C with a flow rate of 0.5 L min^{-1} and 200 psi back pressure.

enhanced performance of the 3D systems is likely driven by the increased AEL|catalyst interface area. Although we attempted to calculate the effects of the 3D junction using numerical simulations, we were unable to draw clear conclusions due to the complexity of the experimental systems and the necessity to simplify aspects of the model in order to achieve convergence in a 2D model (See Supplementary Information for details). Nonetheless, the simulations confirmed that the introduction of 3D junctions greatly affects the water dissociation and formation reaction rates by increasing the high field interfacial area and the number of catalyst sites, supporting our experimental findings. Further optimization of the microstructure could potentially increase the number of active catalytic sites, leading to improved performance.

In a few experimental trials, the 2D BPMs delaminated after dissembling the cell due to water accumulation and swelling in the junction during forward bias testing. In contrast, the 3D BPMs showed no signs of delamination or cracking under forward bias conditions. The better durability may be attributed to the membrane pillars that effectively hold the catalyst nanoparticles in place, preventing them from being washed away by fluid flow or electromigration (Figure S5, Supporting Information). Under forward bias, when the water-formation reaction dominates in the junction, it is crucial for H^+ and OH^- ions to rapidly transport from the bulk membranes into the junction, where they recombine at a high rate. This process can promote delamination, but no delamination was observed in the 3D BPMs. Therefore, we can conclude that the introduction of the 3D structures not only reduces the overpotential for water dissociation and formation reactions but also enhances the mechanical stability of the BPMs.

2.2. H_2-O_2 Fuel Cell Tests

To probe the impact of a controlled 3D BPM interface on electrochemical performance in a technologically relevant energy application, especially where 2D BPMs typically underperform, a final set of experiments was conducted using 3D BPMs as the solid electrolyte in a fuel cell.[42–44] In our tests, humidified H_2 was supplied to the anode, a catalyst-coated gas diffusion layer that was in contact with the CEL layer of the BPM. On the cathode side, humidified O_2 flowed to another catalyst-coated gas-diffusion layer in contact with the AEL. OH^- ions generated from the oxygen reduction reaction at the alkaline cathode migrates through the AEL toward the BPM junction, and H^+ generated from the hydrogen oxidation reaction at the acidic anode migrates through the Nafion toward the junction, ultimately forming water at the AEL|CEL interface.[44,45] Detailed assembly information can be found in the Methods section, and the fuel-cell configuration is schematically illustrated in Figure S6c (Supporting Information).

BPM fuel cell polarization and power-density curves are displayed in **Figure 7**. The peak power density reached a maximum of 184 mW cm^{-2} for the 3.0 × BPM, without IR correction, while the minimum was 20 mW cm^{-2} for a 2D BPM. The 3D BPM achieved a maximum current of 1500 mA cm^{-2} while the 2D counterpart had a limiting current density of 200 mA cm^{-2}. The 3.0 × BPM fuel cell has the potential to achieve a record-breaking performance if other resistances are systematically minimized in the future.

To rationalize the mechanism by which the 3D BPM fuel cell outperformed its 2D counterpart, we can use similar reasoning to our previous discussion of the forward-bias forminggas tests. In the forward-bias fuel-cell condition, H^+ and OH^- must be generated at the anode and cathode, respectively, and these ions need to rapidly transport to the junction. Additionally, H^+ and OH^- must combine to form water at the junction, which then must back-diffuse to the electrodes to avoid swelling and maintain hydration and high ionic conductivity at both the anode and cathode. Rather than observing a mass-transport limit, which would manifest as a plateau in current density at the high current portion of the polarization curve, we see a linear voltage-current density relationship indicative of the ohmic regime (Figure 7a). This makes it unlikely that an insufficient supply of ions or accumulation of water caused the difference in activity between the 2D and 3D BPMs.

Given the earlier onset of current observed in the 3D BPMs, we hypothesize that at a given bias voltage, water formation likely occurs at the same rate on a molecular scale in both 2D and 3D BPMs. However, due to the larger reaction volumes at the structured interfaces of the 3D BPMs, the overall current from water formation is larger. Additionally, the 3D junction may experience more hydration than the 2D junction, which could enhance the back diffusion of water from the internal junction to the

cathode. This could translate to the lower resistance we observe in 3D BPMs for two reasons. First, ion migration may occur more rapidly through the water channels of the ion exchange membranes since the channels are better humidified.[46] It is also possible that there is a lower charge transfer resistance for the oxygen reduction reaction at the cathode, which is the electrode that requires water to generate OH^- ions. Several competing water transport phenomena such as hydraulic pressure, osmotic pressure, and Maxwell forces have been identified in the theoretical BPM literature.[10,47] Future studies using our 3D BPM platform could help to experimentally test the effects of these complex water interactions.

Although these BPMs did not attain the highest performance yet reported for BPM fuel cells,[45,48] which may be due to the presence of ionomer in the catalyst layer as described in the previous section, membrane thickness, and the use of catalyst-coated gas-diffusion layers,[49] they are useful in understanding the viability of 3D BPMs in fuel cells. Future studies should enable observation of the mass-transport-limited regime of 3D BPM fuel cells, giving insight into how the 3D junction manages water accumulation and what power densities an optimized device might be able to achieve.

EIS measurements were performed at both OCV and -200 mA cm^{-2} for all fuel cells, as shown in Figure S11b,c (Supporting Information). The results illustrate a trend in which the diameter of the high-frequency semicircle decreases as the interfacial area of the BPM increases. Since the anode and cathode of each BPM are nominally identical, we hypothesize that this semicircle corresponds to the impedance associated with the water-formation reaction, a diagnosis supported by other studies.[48,50,51] Because this semicircle dominates the impedance of the system, we can conclude that the BPM fuel cell is predominantly limited by the impedance of the water-formation reaction at low current density. The 3D BPM provides more reaction sites for the performance-limiting process to occur leading to substantial improvement in junction conductivity to the point that a new impedance feature begins to dominate the system at low frequency (Figure S11, Supporting Information). While the diagnosis of the low-frequency BPM feature is beyond the scope of this work, we hypothesize that, because its appearance does not seem to vary with the interfacial area of the BPM, it could report on catalysis or mass transfer at the anode and/or cathode. It is promising that 3D structuring of the BPM fuel cell junction can minimize the interfacial resistance to the point where other impedances become dominant in the cell. This discovery suggests that forward-bias BPM fuel cells could be competitive with well-studied monopolar membrane fuel cells while benefiting from a self-humidifying junction.

As shown in Figure S12 (Supporting Information), the resistance decreased with increasing interfacial area, and we also observed that the capacitance of the bipolar membrane junction increased linearly with increasing interfacial surface area. This behavior supports the interpretation of the high-frequency semicircle as representative of the BPM junction and validates our controlled fabrication method. If we treat the BPM junction as a parallel plate capacitor, capacitance should scale directly with the area of each side of the BPM as it does in these measurements.

A series of EIS measurements of the 3.0 × BPM fuel cell at different current densities is presented in Figure S11a (Supporting Information). To better understand the changes in resistance and water formation in the bipolar junction region, EIS was carried out at intervals of 200 mA cm^{-2}. The high-frequency semicircle representing water formation gradually disappears as current density is increased beyond 400 mA cm^{-2}. This current regime coincides with the transition of the polarization curve from exponential to linear (Figure 7a), suggesting that the water formation reaction is adequately driven. It is possible that current is now limited by electron transfer kinetics at the electrodes and/or ionic migration through the membrane bulk, but confirmation of these hypotheses would require additional electrochemical measurements.

We also tested BPMs without catalyst under identical conditions, resulting in the anticipated inferior performance compared to BPMs with catalyst (Figure 7b). In this scenario, the highest power density achieved was only 34.2 mW cm^{-2} for the 3.0 × BPM, while the 2D BPM reached only 20 mW cm^{-2}. Despite the low performance of these non-catalyst BPMs, a consistent trend persisted that 3D BPMs achieved higher power density, operated in a wider current density range, and exhibited lower resistance according to EIS plots compared to 2D BPMs. While the catalyst-free BPM performance is not relevant to fuel-cell applications, it highlights the importance of engineering high-activity catalysts for both the water dissociation and formation reactions. Additionally, it is noteworthy that the 2D BPM with ACB/TiO_2 performs approximately the same as the 2D BPM without a catalyst, suggesting that the 2D BPM fuel cell is not limited by the absence of a water-formation catalyst but likely by the reaction volume in which water formation can take place. The anatase TiO_2 used in this study has been shown to be an effective catalyst for water formation in BPMs.[22] We conclude that although our water-formation catalyst has high activity, the 2D BPM junction lacks sufficient reaction volume to observe a significant catalytic enhancement in water-formation current density. It seems that a larger interfacial area is needed before the addition of a water-formation catalyst can enhance the water-formation rate in the fuel cell. Although the catalyst layer prevents complete binding of the AEL and CEL in all catalyzed samples, the 3D BPMs benefit from having a more interfacial area for reactions to occur.

When comparing EIS measurements of the catalyzed BPM (Figure S11b,c, Supporting Information) to those of the non-catalyzed BPM (Figure S13, Supporting Information) at the same current density, the catalyzed BPMs exhibit substantially lower resistance in the BPM junction, indicated by the smaller diameter of the first semicircle. This is likely due to the catalyst's ability to enhance water formation to a certain degree, which is critical for improving the performance of the BPM fuel cell.

3. Conclusion

A geometrically controlled nano-/micropatterned 3D BPM with a quantifiable junction area was successfully fabricated and tested. The feature size was in a dimension that was very relevant to the catalysis study. The performance of BPMs can be improved by increasing the interfacial junction catalysis area through soft lithography. While these 3D BPMs have not yet achieved record-breaking performance, there is a clear trend and rationale for improving 3D BPMs relative to their 2D counterparts under both forward/reverse-bias conditions. This trend holds promise for

the advancement of BPM applications in the future with optimized materials and conditions. Future studies on 3D BPMs fuel cells could emphasize low humidity conditions because of their inherent self-humidification property. Moreover, they could explore the application of less precious metal catalysts, enabled by the separation of acidic and alkaline pH conditions at the anode and cathode, respectively.

4. Experimental Section

Materials: The mTPN1 polymer was synthesized as described elsewhere.[35] The CEL Nafion NR-212 was purchased from Ion Power, Inc. and the CEL ionomer was the 5wt% Nafion 117 from Sigma–Aldrich. Materials for producing micropattern silicon wafer templates and corresponding PDMS molds were 3 µm Polybead Hydroxylate Microspheres from Polysciences, Inc., silicon wafer (525 µm in thickness) from University Wafer. Inc., 1H,1H,2H,2H-Perfluorooctyltrichlorosilane (97%) from Alfa Aesar, and PDMS Sylgard 184 Silicone Elastomer Base and Curing Agent from Electron Microscopy Sciences. Other chemicals and materials include dimethyl sulfoxide (DMSO) and isopropanol from Fisher Scientific, 1-propanol and N-methyl-2-pyrrolidone (NMP) from Acros Organics, ethanol 200 Proof from Decon Laboratories, Inc., titanium dioxide nanopowder (TiO_2, Anatase, 99.98%, 30 nm) from US Research Nanomaterials, Inc., tin oxide,[39] silicon dioxide (nanopowder, 99.5%, 10–20 nm) from Sigma-Aldrich, carbon black (acetylene, 50% compressed, 99.9+%) from Alfa Aesar, potassium hydroxide from Macron Fine Chemicals, and Airbrush from PointZero. Additionally, high-surface-area platinum black, Sigracet carbon paper, and Teflon in 0.02″, 0.005″, and 0.002″ thickness all came from the Fuel Cell Store. Nanopure water with 18.2 MΩ resistivity was used. Instruments include Ender 3D printer from Creality 3D Technology Co., Ltd., Model 850e Fuel Cell Test System from Scribner, Autolab Potentiostat (PGSTAT128N) from Metrohm, and DC Power Supply E3612A from Agilent.

Methods—Nano-/Micro-Fabrication of the 3D Anion Exchange Layer (3D AEL): An example of making a nano-/micropatterned template is shown below. A polystyrene particle solution was prepared by diluting the stock 3 µm (or any other size of particles ranging from 200 nm to 4.5 µm) polystyrene particle solution with an equal volume of ethanol. A glass petri dish (freshly base bath or plasma cleaned) was partially filled with nanopure water, leaving a small island of exposed glass surface. The polystyrene particle mixture was added dropwise onto the glass area. As the particle solution spread, the water gradually contacted the solution, scooped up the particles, and formed a monolayer at the air-water interface. A wet hydrophilic silicon wafer, pre-cleaned with piranha solution, was inserted into the water at a slight angle, allowing the monolayer to gradually climb up and uniformly cover the wafer's surface.

The polystyrene particles were uniformly shrunk through exposure to O_2 plasma, creating gaps between the particles. The reactive ion etcher was operated at a power of 90 W with 40 sccm O_2 flow for 9 min. The exposed silicon area was then vertically etched by applying SF_6 plasma through deep reactive ion etching. The remaining polystyrene particles on the silicon surface were removed by either etching with O_2 plasma or by dissolving in N-methylpyrrolidone (NMP) with gentle sonication (Figure S1, Supporting Information).

1H,1H,2H,2H-Perfluorooctyltrichlorosilane was deposited on the patterned silicon wafer surface through vapor deposition to make the silicon wafer surface highly hydrophobic. Subsequently, the silicon template was affixed to aluminum foil and folded into a cubic boat-like shape. A PDMS solution, with a base-to-curing agent ratio of ≈12:1, was poured onto the silicon template until it filled the aluminum foil boat, and the vessel was vacuumed in a desiccator for ≈30 min to remove any air from the PDMS solution, allowing the PDMS to gradually fill the pores in the silicon template. The PDMS mold was then easily peeled off from the silicon wafer after solidifying in an oven at 70 °C for 2 h. This process yielded an easily reproducible and reusable PDMS mold with geometrically controlled structures (Figure S2, Supporting Information).

The AEL solution was prepared by dissolving the mTPN1 polymer powder in DMSO to make a 7 wt.% solution. The vial was sonicated for ≈20 min until a clear, viscous, light orange solution was obtained. The surface of the PDMS mold was plasma-cleaned and a specific quantity of the AEL solution was pipetted on. For instance, applying 280 µL of a 7 wt.% mTPN1 solution on a 2 × 2 cm^2 mold would result in a 42 ± 3 µm thick membrane after baking. The assembly was then placed in a vacuum desiccator to allow the AEL solution to gradually infiltrate the holes. After ≈20 min, the assembly was carefully removed from the desiccator and placed on a hotplate at 60 °C for 2 h before being transferred to a 70 °C oven overnight to evaporate any remaining organic solvent.

After the baking process was completed, the assembly was placed inside a chamber along with a humidifier to allow water vapor to gradually moisten the membrane, making it easier to peel the AEL off from the PDMS.

Methods—Preparation of Bipolar Membranes (BPMs): After removal from the PDMS, the AELs were pretreated by soaking in 1 M KOH for ≈5 h before use. Subsequently, the membrane was rinsed with water and gently patted dry with a paper towel.

The catalyst was sprayed on the surface of the structured AEL. A stock ink of 0.4 wt.% of 30 nm anatase TiO_2 or 5 nm SnO_2 in isopropanol (IPA) was prepared. An equivalent weight percent of acetylene carbon black (ACB) was added to the mixture (MO_2/ACB = 100% w/w), and the mixture was horn sonicated for ≈20 min or until the particles were well dispersed. The stock ink was then diluted with IPA to achieve a 0.04 wt.% MO_2/ACB solution. A specific quantity of 5 wt.% Nafion in alcohol was chosen as the ionomer to be added to the catalyst until the mass of the ionomer reached 20% of the MO_2 mass. This ink was sonicated for ≈20 min and was ready for spraying.

The pretreated AEL was placed on a hotplate and vacuumed from the bottom to ensure it was flat and dry, exposing an area of 1.5 × 1.5 cm^2. The hotplate was maintained at a temperature of ≈30 °C. The diluted ink was carefully sprayed onto the AEL using a homemade auto-sprayer. The spraying area was 1.05 × 1.05 cm^2. In our experiment, 300 mg of a 0.04 wt.% MO_2/ACB solution was evenly sprayed on the AEL in ≈15 min. Once the ink had dried, the entire membrane was submerged in a falcon tube filled with 1 M KOH solution in a 70 °C oven overnight.

Nafion 212 was employed as the CEL. The Nafion membranes underwent activation through a series of steps. First, they were cut into 2 × 2 cm^2 squares and soaked in 3% H_2O_2 at 80 °C for 1 h. Then, the membranes were immersed in water for an additional h at 80 °C, followed by heating in 1 M H_2SO_4 at the same temperature for another hour. The membranes were thoroughly washed with nanopure water between each step. The activated Nafion membranes were stored in 1 M H_2SO_4 at room temperature. Nafion was thoroughly rinsed with water and carefully dried prior to use.

Following the overnight soaking of the AEL in KOH, the AEL was rinsed with water and gently dried. With the catalyst side facing up, a Nafion film was placed on top of it. This assembly was sandwiched between Teflon sheets (outer layer 0.02″, inner layer 0.002″) and underwent hot-press at 165° with a pressure of 2.5 metric tons for 25 min to form a complete BPM for the tests.

Methods—Preparation of Gas Diffusion Layer (GDL) and the Cell: The ink was prepared in a 4 mL scintillation vial, consisting of 24 mg of Pt black in 3 mL propanol. For the GDL on the AEL side, a 7 wt% mTPN1 in DMSO ionomer was used, while a 5 wt.% Nafion in DMF ionomer was employed on the CEL side. The ink was sonicated for ≈20 min or until all the particles were well dispersed. The substrate for the GDL was carbon paper Sigracet 28 BC. A vial of ink was uniformly spray-coated onto a square of 3.45 × 3.45 cm^2 of carbon paper while the paper was vacuum-sealed on a hotplate at ≈90 °C. Subsequently, the GDL was cut into 1.0 × 1.0 cm^2 squares for later use. The AEL GDL was soaked in 1 M KOH for 2 h before use.

The MEA design applied in this study was inspired by previous research.[22,52] The Teflon gaskets used in this assembly had an active area of 1.0 × 1.0 cm^2. To assemble the cell, a Teflon gasket was placed on top of the CEL flow field. The CEL GDL was positioned in the square hole of

the gasket with the Pt side facing upward, followed by the BPM with the CEL side in contact with the CEL GDL. Then, another Teflon gasket with a square hole was placed on top of the BPM. The AEL GDL was inserted into the hole with the Pt facing down to let the Pt get in contact with the AEL. Finally, another piece of the flow field was carefully aligned with the assembly, and all the pieces were bolted together. The screws were tightened by applying 6.2 Nm of torque using a torque wrench.[23] Whether forming gas was used or H_2-O_2 was used, gases were humidified by nanopure water before flowing to the cathode and anode.

Methods—Polarization Behavior of BPMs: For each BPM with a given surface area, at least three trials of polarization tests were performed to ensure reproducibility. For the forming gas test, both the cell and fuel temperatures were set to 60 °C, and the flow rates of the gases on both sides were maintained at 0.5 L min^{-1}. The system was allowed to stabilize at 0 mA cm^{-2} for ≈30 min before testing started. Then the current density was gradually stepped up, with each step being held until the potential stabilized.[23] Once the current density reached ≈120 mA cm^{-2}, the current density was then systematically decreased in reverse order. The potential at each current density step was recorded, and at least three cycles of up-and-down were performed. The reported polarization curves were constructed from the average potentials measured during each current step of at least three trials. Electrochemical-impedance-spectroscopy (EIS) measurements were recorded at certain current density steps, beginning with the highest current density and moving downward. The AC amplitude was set to 0.001 A. The frequency was scanned from 100 kHz to 50 or 0.1 Hz. The data in the higher frequency region were associated with water dissociation/formation and were fitted by a simple Randles circuit to obtain the series resistance (R_s), water dissociation resistance/formation (R_{wd}), and water dissociation/formation capacitance (C_{wd}).

For the fuel-cell tests, the cell temperature was maintained at 100 °C, and the fuel temperature was set to 99 °C, with a consistent gas flow rate of 0.5 L min^{-1}. Tests were also conducted at 60 °C but the cell performed better at 100 °C. The back pressure was set to 200 psi. The current density was progressively introduced to the system until the potential dropped to zero. This procedure was repeated until the system's performance (e.g., peak power density, or current density range) either stabilized or began to decay. At least three trials of experiments were conducted for each scenario. The performance of a set of membranes was reported in the main text as an example. EIS measurement was conducted after the completion of the test. The procedures and analysis for the fuel cell tests were identical for the BPMs with no catalyst.

Supporting Information

Supporting Information is available from the Wiley Online Library or from the author.

Acknowledgements

This work was primarily supported by the U.S. Department of Energy, Office of Science Energy Earthshot Initiative as part of the Center for Ion Management in Electrochemical Systems (CIMES) under Award DE-SC0024713. This work was also supported by the Vagelos Institute for Energy Science Technology at the University of Pennsylvania. Characterization studies were carried out in part at the Singh Center for Nanotechnology at the University of Pennsylvania, which is supported by the NSF National Nanotechnology Co-ordinated Infrastructure Program under grant NNCI-2025608. T. G. and L. S. would like to acknowledge the Vagelos Institute for Energy Science and Technology at the University of Pennsylvania for a graduate fellowship and for a postdoctoral fellowship, respectively. C.J.S. would like to acknowledge the National Science Foundation Graduate Research Fellowship Program (NSF GRFP, DGE1845298).

Conflict of Interest

The authors declare no conflict of interest.

Data Availability Statement

The data that support the findings of this study are available in the supplementary material of this article.

Keywords

3D bipolar membrane, bipolar interface, bipolar membrane, bipolar membrane fuel cell, metal oxide catalyst, water dissociation, water formation

Received: September 18, 2024
Revised: October 29, 2024
Published online:

[1] M. A. Blommaert, D. Aili, R. A. Tufa, Q. Li, W. A. Smith, D. A. Vermaas, *ACS Energy Lett.* **2021**, *6*, 2539.
[2] T. Xu, *J. Membr. Sci.* **2005**, *263*, 1.
[3] C. Qiu, Z. Xu, F. Y. Chen, H. Wang, *ACS Catal.* **2024**, *14*, 921.
[4] S. Hao, H. Sheng, M. Liu, J. Huang, G. Zheng, F. Zhang, X. Liu, Z. Su, J. Hu, Y. Qian, L. Zhou, Y. He, B. Song, L. Lei, X. Zhang, S. Jin, *Nat. Nanotechnol.* **2021**, *16*, 1371.
[5] P. K. Giesbrecht, M. S. Freund, *Chem. Mater.* **2020**, *32*, 8060.
[6] S. J. Oener, M. J. Foster, S. W. Boettcher, *Science* **2020**, *369*, 1099.
[7] S. Kole, G. Venugopalan, D. Bhattacharya, L. Zhang, J. Cheng, B. Pivovar, C. G. Arges, *J. Mater. Chem. A* **2021**, *9*, 2223.
[8] Z. Yan, R. J. Wycisk, A. S. Metlay, L. Xiao, Y. Yoon, P. N. Pintauro, T. E. Mallouk, *ACS Cent. Sci.* **2021**, *7*, 1028.
[9] M. B. McDonald, S. Ardo, N. S. Lewis, M. S. Freund, *ChemSusChem* **2014**, *7*, 3021.
[10] J. C. Bui, E. W. Lees, D. H. Marin, T. N. Stovall, L. Chen, A. Kusoglu, A. C. Nielander, T. F. Jaramillo, S. W. Boettcher, A. T. Bell, A. Z. Weber, *Nature Chemical Engineering* **2024**, *1*, 45.
[11] J. Ran, L. Wu, Y. He, Z. Yang, Y. Wang, C. Jiang, L. Ge, E. Bakangura, T. Xu, *J. Membr. Sci.* **2017**, *522*, 267.
[12] X. Zhang, C. Ye, K. Pi, J. Huang, M. Xia, A. R. Gerson, *Sep. Purif. Technol.* **2019**, *211*, 330.
[13] Y. Zhao, L. Wang, Z. Ji, J. Liu, X. Guo, F. Li, S. Wang, J. Yuan, *Desalination* **2020**, *494*, 114654.
[14] S. Chabi, K. M. Papadantonakis, N. S. Lewis, M. S. Freund, *EES* **2017**, *10*, 1320.
[15] J. K. Lee, F. Babbe, G. Wang, A. W. Tricker, R. Mukundan, A. Z. Weber, X. Peng, *Joule* **2024**, *8*, 2357.
[16] E. W. Lees, J. C. Bui, D. Song, A. Z. Weber, C. P. Berlinguette, *ACS Energy Lett.* **2022**, *7*, 834.
[17] J. C. Bui, É. Lucas, E. W. Lees, A. K. Liu, H. A. Atwater, C. Xiang, A. T. Bell, A. Z. Weber, *EES* **2023**, *16*, 5076.
[18] A. W. Tricker, J. K. Lee, F. Babbe, J. R. Shin, A. Z. Weber, X. Peng, *ACS Energy Lett.* **2023**, *8*, 5275.
[19] A. Ter Heijne, H. V. M. Hamelers, V. De Wilde, R. A. Rozendal, C. J. N. Buisman, *Environ. Sci. Technol.* **2006**, *40*, 5200.
[20] J. C. Bui, K. R. M. Corpus, A. T. Bell, A. Z. Weber, *J. Phys. Chem. C* **2021**, *125*, 24974.
[21] Z. Yan, T. E. Mallouk, *Acc. Mater. Res.* **2021**, *2*, 1156.
[22] J. B. Mitchell, L. Chen, K. Langworthy, K. Fabrizio, S. W. Boettcher, *ACS Energy Lett.* **2022**, 3967.
[23] L. Chen, Q. Xu, S. Z. Oener, K. Fabrizio, S. W. Boettcher, *Nat. Commun.* **2022**, *13*, 3846.
[24] C. Shen, R. Wycisk, P. N. Pintauro, *EES* **2017**, *10*, 1435.
[25] Y. L. Kao, L. Chen, S. W. Boettcher, D. Aili, *ACS Energy Lett.* **2024**, 2953.
[26] J. Pan, L. Hou, Q. Wang, Y. He, L. Wu, A. N. Mondal, T. Xu, *Mater. Chem. Phys.* **2017**, *186*, 484.

[27] Z. Yan, L. Zhu, Y. C. Li, R. J. Wycisk, P. N. Pintauro, M. A. Hickner, T. E. Mallouk, *EES* **2018**, *11*, 2235.
[28] E. Al-Dhubhani, H. Swart, Z. Borneman, K. Nijmeijer, M. Tedesco, J. W. Post, M. Saakes, *ACS Appl. Energy Mater.* **2021**, *4*, 3724.
[29] Y. Chen, J. A. Wrubel, W. E. Klein, S. Kabir, W. A. Smith, K. C. Neyerlin, T. G. Deutsch, *ACS Appl. Polym. Mater* **2020**, *2*, 4559.
[30] E. Al-Dhubhani, M. Tedesco, W. M. de Vos, M. Saakes, *ACS Appl. Mater. Interfaces* **2023**, *15*, 45745.
[31] Y. Jeon, D. J. Kim, J. K. Koh, Y. Ji, J. H. Kim, Y. G. Shul, *Sci. Rep.* **2015**, *5*, 16394.
[32] J. W. Bae, Y. H. Cho, Y. E. Sung, K. Shin, J. Y. Jho, *J. Ind. Eng. Chem.* **2012**, *18*, 876.
[33] Z. Zhou, R. N. Dominey, J. P. Rolland, B. W. Maynor, A. A. Pandya, J. M. DeSimone, *J. Am. Chem. Soc.* **2006**, *128*, 12963.
[34] S. Jang, M. Her, S. Kim, J. H. Jang, J. E. Chae, J. Choi, M. Choi, S. M. Kim, H. J. Kim, Y. H. Cho, Y. E. Sung, S. J. Yoo, *ACS Appl. Mater. Interf.* **2019**, *11*, 34805.
[35] W. H. Lee, E. J. Park, J. Han, D. W. Shin, Y. S. Kim, C. Bae, *ACS Macro Lett.* **2017**, *6*, 566.
[36] A. Raut, H. Fang, Y. C. Lin, D. Sprouster, Y. Yin, Y. Fang, S. Fu, S. Sharma, L. Wang, C. Bae, M. Rafailovich, *Energy Adv.* **2023**, *2*, 113.
[37] Y. Yang, H. Peng, Y. Xiong, Q. Li, J. Lu, L. Xiao, F. J. Disalvo, L. Zhuang, H. D. Abrunã, *ACS Energy Lett.* **2019**, *4*, 1251.
[38] A. S. Metlay, Y. Yoon, L. Schulte, T. Gao, T. E. Mallouk, *ACS Appl. Energy Mater.* **2024**, *7*, 7125.
[39] S. Sasmal, L. Chen, P. V. Sarma, O. T. Vulpin, C. R. Simons, K. M. Wells, R. J. Spontak, S. W. Boettcher, *Nat. Mater.* **2024**, *23*, 1421.
[40] C. G. Rodellar, J. M. Gisbert-Gonzalez, F. Sarabia, B. Roldan Cuenya, S. Z. Oener, *Nat. Energy* **2024**, *9*, 548.
[41] L. Schulte, W. White, L. A. Renna, S. Ardo, *Joule* **2021**, *5*, 2380.
[42] X. Xu, S. Peng, S. Lu, J. Gong, J. Zhang, W. Huang, Y. Xiang, *J. Power Sources* **2017**, *354*, 92.
[43] C. G. Arges, V. Prabhakaran, L. Wang, V. Ramani, *Int. J. Hydrogen Energy* **2014**, *39*, 14312.
[44] M. Ünlü, J. Zhou, P. A. Kohl, *J. Phys. Chem. C* **2009**, *113*, 11416.
[45] S. Peng, X. Xu, S. Lu, P. C. Sui, N. Djilali, Y. Xiang, *J. Power Sources* **2015**, *299*, 273.
[46] K. A. Mauritz, R. B. Moore, *Chem. Rev.* **2004**, *104*, 4535.
[47] K. N. Grew, W. K. S. Chiu, *J. Electrochem. Soc.* **2020**, *167*, 164513.
[48] D. Seeberger, D. McLaughlin, P. Hauenstein, S. Thiele, *Sustain. Energ. Fuels* **2020**, *4*, 2508.
[49] H. Tang, S. Wang, S. P. Jiang, M. Pan, *J. Power Sources* **2007**, *170*, 140.
[50] K. N. Grew, J. P. McClure, D. Chu, P. A. Kohl, J. M. Ahlfield, *J. Electrochem. Soc.* **2016**, *163*, F1572.
[51] X. Yuan, H. Wang, J. Colin Sun, J. Zhang, *Int. J. Hydrogen Energy* **2007**, *32*, 4365.
[52] F. Afsahi, F. Mathieu-Potvin, S. Kaliaguine, *Fuel Cells* **2016**, *16*, 107.